

Image sharpness metric-based deformable mirror control for beam projection systems operating in strong scintillation

Ronald Kizito, Michael C. Roggemann, Tim Schulz and Yanchai Zhang

Department of Electrical Engineering, Michigan Technological University,
1400 Townsend drive, Houghton, Michigan 49931 USA

ABSTRACT

We describe a new approach to controlling the deformable mirror in beam projection systems operating in conditions of strong scintillation. Under the conditions of interest, two-way propagation is required to create the light used for wavefront sensing. In this situation, the beacon can subtend an angle that is many times larger than the isoplanatic angle. Our approach uses a nonlinear optimization-based technique to determine the deformable mirror (DM) figure which optimizes an image sharpness metric. This correction is applied to the outgoing laser beam with the goal of concentrating most of the laser's power on a small area of the target. The optimization algorithm chosen for this purpose is the simultaneous perturbation stochastic approximation (SPSA). Our results show that using phase-only conjugation with nonlinear optimization of an image sharpness metric can provide an improvement in encircled energy performance compared to phase-only conjugation with only linear Hartman wavefront sensor processing.

Keywords: phase conjugation, scintillation, nonlinear optimization, extended beacons

1. INTRODUCTION

Many laser projection systems, such as those found in laser weapon systems and laser communication systems, have the goal of focusing a laser beam on a target through a long atmospheric path. The objective in these systems is often to concentrate as much power as possible on a small area of the target. In long range air-to-air laser projection systems, the laser beam must propagate almost horizontally through atmospheric turbulence. In the absence of atmospheric turbulence, the beam reaching the target would have a high power density and an almost Airy-disk pattern as predicted by diffraction theory. However, in conditions of strong atmospheric turbulence, the amplitude and phase of the laser beam are severely distorted as the beam propagates through the long optical path.¹⁻³ Therefore the beam reaching the target in general has a low power density, and its intensity pattern is randomly changing and speckled in appearance.^{4,5}

A laser beacon-based adaptive optics system provides a way to correct for the turbulence-induced phase distortion.¹ In this system, a beacon is created by transmitting one or more low power laser beams from the laser projection system to the target. Some of the light from the beacon scatters back through the atmosphere and is captured by the aperture of the laser projection system. Assuming that all the sources of the scattered light captured by the aperture of the laser projection system emanate from a very small region of the target, conventional adaptive optics systems can lead to a significant improvement in performance. Ideally, to compensate for weak phase distortions, the conjugate of the phase of the beacon field incident on the aperture is applied to the outgoing beam. In practice, the phase conjugation is performed by controlling the shape of a reflective deformable mirror. The deformable mirror is in turn controlled through a set of 'actuator control' weights obtained processing either wavefront sensor information,² image information,⁶ or both.^{7,8} Assuming weak turbulence, and that the outgoing laser beam propagates through roughly the same optical path as the scattered light, the beam reaching the target will approach diffraction-limited performance.

Unfortunately, the approach described above works well only in cases where the atmospheric turbulence is weak and the beacon is a point source. In beam projection systems operating in conditions of strong atmospheric turbulence, the amplitude and phase of the field incident on the target are severely distorted, and the target itself is extended. Therefore, the beacon that is created is not a point source, but rather it is a randomly shaped, extended source. Because the beacon field is scattered by an optically rough surface, the beacon is also spatially incoherent. Hence, in most cases of practical interest the beacon subtends an angle that is many times larger than

the isoplanatic angle so that the beacon looks like a collection of several small isoplanatic patch-sized regions. The scattered light from each one of these regions goes through a slightly different volume of turbulence and experiences different amplitude and phase distortions. Hence the field incident on the aperture originates from different isoplanatic patch-sized regions of the beacon, and this total field causes the image and Hartman sensor data we would measure. The various random point spread functions arising from different parts of the beacon are super-imposed in both the image and Hartman sensor data. Simply conjugating the phase estimated from the Hartman sensor and image data, and applying it to the outgoing laser beam is not as effective as finding a means to isolate and conjugate the phase associated with a small patch on the target. The approach we describe later in this paper provides a way to reduce the errors related to what we call “beacon anisoplanatism”. In addition to the anisoplanatism described above, the beacon field experiences strong scintillation because of the long optical paths through which it propagates. However, the approach described in this paper is a phase conjugation scheme and does not compensate for amplitude errors. However, we will show that phase-only correction is still very useful.

Most previous work in this area has involved the use of the entire scattered field incident on the aperture in order to find the optimum control weights to apply to the deformable mirror. For instance, Roggemann et al. describe a nonlinear optimization-based technique to determine the deformable mirror figure which jointly processes Hartman sensor and image data to obtain commands for a deformable mirror.^{7,8} We have found that his approach provides only small improvements in percentage of encircled energy when the beacon is extended, and is very computationally intensive.

In this paper, we describe an approach that is based on a modified version of the laser beacon and phase-conjugation adaptive optics system. As shown in figure 1, instead of using all the scattered light from the beacon, we have developed a measurement and processing technique that seeks to use a small portion of the light emanating from a small patch on the beacon. This patch subtends an angle that is only a few times larger than the isoplanatic angle and forms the basis for the image sharpness metric. The image sharpness metric used here was first described by Muller and Buffington et al.^{9,10} and was later used by Voronstov, et al.⁶ This image sharpness metric is given by

$$J(\alpha) = \int M(\mathbf{x})I(\mathbf{x};\alpha)d^2\mathbf{x}, \quad (1)$$

where \mathbf{x} is the position vector in the image plane, $M(\mathbf{x})$ is a mask which blocks the light from some regions of the image plane, $I(\mathbf{x})$ is the image intensity due to the beacon, and α s are the DM actuator commands. As we mentioned above, the image intensity contains components from several isoplanatic patch-sized regions. Therefore a spatial filter, in this case the mask, $M(\mathbf{x})$, with a small circular aperture is used as a field stop to pass only light from a small region of the target to the optimization technique suggested by Eq. (1). If the diameter of the mask aperture subtends an angle that is a few times larger than the isoplanatic angle, we can effectively compensate for an almost isoplanatic patch-sized portion of the target by iterating on the elements of α . The deformable mirror then performs the necessary phase correction to the outgoing high power laser. Several optimization algorithms such as the BFGS quasi-Newton method^{11,12} or the SPSA¹³ can be used to find the optimum values of α that maximize the image sharpness metric, J . However, we used the SPSA because of its convergence speed.

So far the results obtained with this approach have been promising. The results from our simulations show that deformable mirror control based on the nonlinear optimization of the image sharpness metric, leads to an improvement in the percentage of encircled energy over previous DM control approaches based on simply conjugating the phase obtained from wavefront sensors and reconstructors. The simulation results also show that ideal mask aperture can subtend an angle that is many times larger than the isoplanatic angle. The simulation results show that in some cases the best angular subtense can be many times the isoplanatic angle.

The rest of the paper is organized as follows. In section 2, we briefly describe the theory behind the beam projection system and we derive a formula that relates the mask aperture’s diameter to its angular subtense. In section 3, we describe the computer simulations that were performed and in section 4, we show the results of the simulations. Section 5, has our conclusions.

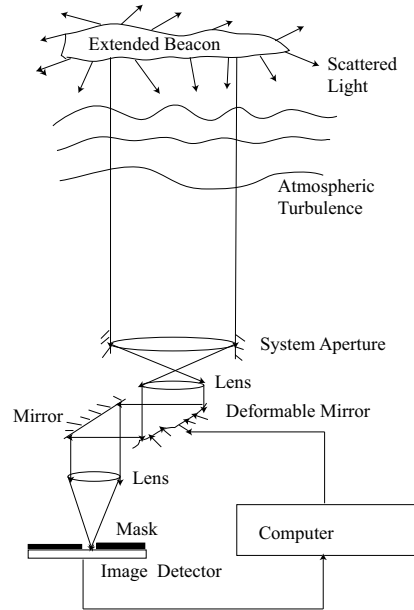


Figure 1. Illustration of the adaptive optical system

2. THEORY

Fig. 1 shows the functional block diagram of the adaptive optical system. The artificial beacon is created by focusing a laser beam from the projection system on the target. Some of the light from the newly created extended beacon scatters back through the atmosphere to the aperture of the beam projection system. A lens in the system aperture focuses the incoming light on to the image plane. Let the field in the system aperture be given by $U_s(\mathbf{x}_s)$, where \mathbf{x}_s is a position vector.

$$U_s(\mathbf{x}_s) = \int h(\mathbf{x}_s, \mathbf{x}_b) U_b(\mathbf{x}_b) d\mathbf{x}_b, \quad (2)$$

where $U_b(\mathbf{x}_b)$ is the beacon field and $h(\mathbf{x}_s, \mathbf{x}_b)$ is the point spread function. Then the field immediately after the lens is given by

$$U_{sl}(\mathbf{x}_s) = U_s(\mathbf{x}_s) \exp\left(-j \frac{k}{2F} \mathbf{x}_s^2\right) P(\mathbf{x}_s), \quad (3)$$

where $P(\mathbf{x}_s)$ is the pupil function, F is the focal length of the lens, and k is the wave number. The focal length, F , is chosen so that in the absence of atmospheric turbulence a collimated beam would be available after the lens. The image plane field is given by

$$U_i(\mathbf{x}_i; \alpha) = \Im\{U_s(\mathbf{x}_s) \exp[-j\Phi_{dm}(\mathbf{x}_a; \alpha)]\}, \quad (4)$$

where $\Phi_{dm}(\mathbf{x}_a; \alpha)$ is the phase correction added to the field by the deformable mirror. The model for the DM figure is

$$\Phi_{dm}(\mathbf{x}_a) = \sum_{k=1}^N \alpha_k b_k(\mathbf{x}_a), \quad (5)$$

where $b_k(\mathbf{x}_a)$ is the set of DM influence functions. The image intensity distribution is given by

$$I_i(\mathbf{x}_i; \alpha) = |U_i(\mathbf{x}_i; \alpha)|^2. \quad (6)$$

The integrated image intensity inside the circular mask was then maximized using the SPSA algorithm. The objective function to be maximized is the discrete version of Eq. (1)

$$J(\alpha) = \sum_{\mathbf{x}_i} I_i(\mathbf{x}_i; \alpha) M(\mathbf{x}_i), \quad (7)$$

where \mathbf{x}_i in this context is a sampled image plane coordinate.

In cases of interest to us, the angular extent of the beacon is many times larger than the isoplanatic angle. Therefore at the aperture, the beacon looks like a collection of many isoplanatic patch-sized sources. To reduce the effects of anisoplanatism we have to pick a patch on the beacon that is a few times larger than the isoplanatic patch and compensate for this patch. We do this by filtering out some of the light from the other isoplanatic patch-sized sources in the beacon. Fig. 2 shows the relationship between the angular subtense, θ_{mask} , and the

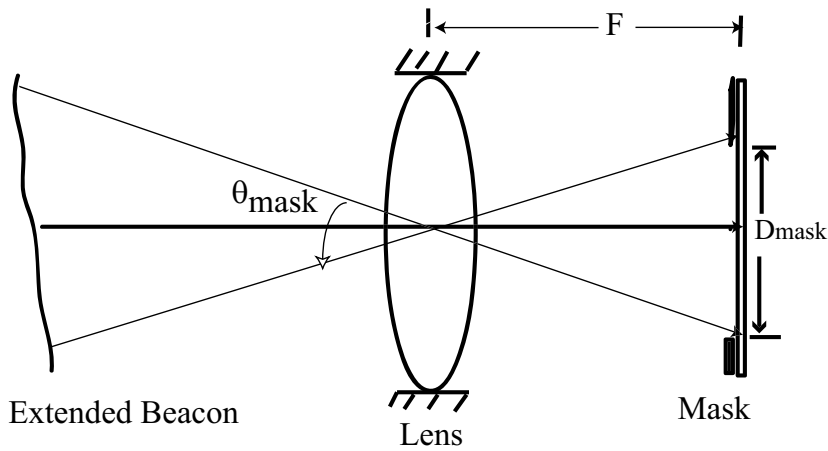


Figure 2. Illustration of the angular extent of the mask's aperture

diameter of the mask's aperture. In the following equations, we show the relationship between the mask diameter and the angle it subtends in the target plane.

$$\theta_{mask} = \frac{D_{mask}}{F}, \quad (8)$$

where F is the focal length of the lens and D_{mask} is the diameter of the mask aperture. Assuming that C_n^2 is a constant, Fried's¹⁴ formula for the isoplanatic angle reduces to

$$\theta_0 = \left[2.91 \frac{3}{8} k^2 C_n^2 z^{8/3} \right]^{-3/5}. \quad (9)$$

The Rytov number, σ_χ^2 , is given by

$$0.5631 k^{7/6} \int_0^z dv C_n^2(v) v^{5/6} \quad (10)$$

A comparison between the isoplanatic angle, angular subtense of the mask diameter and the angular subtense of the beacon were made and the results presented in a table in section 4.

3. SIMULATION DESCRIPTION

Analytical solutions to the propagation of laser projection systems under conditions of strong atmospheric turbulence are not available. Therefore, we used the Monte Carlo method to simulate several independent optical propagations. We used the percentage of encircled energy in the ensemble average target intensity and the radial energy in the ensemble average target intensity as the performance metrics. Each simulation can be broken down into several parts. The first part is the creation of the extended beacon of wavelength, $\lambda = 980$ nm. The second part is the propagation of the scattered extended beacon wavefronts from the target plane to the aperture of the laser beam projection system. In the next part we form an image of the field in the system aperture and then optimize the image sharpness metric described above. Finally, we correct the phase of the outgoing high power laser beam.

The extended beacon was created by propagating a Gaussian beam to a target at a simulated distance, z , of 10 km. In our simulations, the target plane was created on a 1024×1024 uniform Cartesian grid. In the simulations, we used a 5-layered atmospheric model. The 5 thin layers were uniformly spaced so that the distance between each thin layer was $\Delta z = 2$ km. The first layer was placed at a distance of 10 km from the beacon plane and the last layer was placed in the aperture plane. Each layer (or phase screen) was created using a phase screen generator.¹⁵ In turn the phase screen was created on a 1024×1024 Cartesian grid with a sample spacing of $\Delta x = 0.568$ cm. This sample spacing meets the Nyquist sampling criterion of $1024 > 2\lambda z/\Delta x^2$. Each phase screen had a von Kármán power spectral density, an outer scale, $L_0 = 10$ m, and an inner scale, $l_0 = 0$ m. We assumed that each phase screen had the same structure constant, C_n^2 . Furthermore, C_n^2 was independent of position and was therefore a constant. The isoplanatic angle, θ_0 , and the Fried parameter, r_0 , change depending on the structure constant.

We used several values of C_n^2 to simulate the effects of different turbulence strengths on the performance of our new system. The following values of C_n^2 were used: $5.7354 \times 10^{-16} \text{ m}^{-2/3}$, $C_n^2 = 9.5591 \times 10^{-16} \text{ m}^{-2/3}$, and $13.383 \times 10^{-16} \text{ m}^{-2/3}$. The Gaussian beam is propagated between any two phase screens using an FFT-based angular spectrum propagator.^{16,17}

To simulate scattering from a finite-sized target, the central portion of the field at the target was extracted. The atmospheric turbulence causes the phase of the scattered field at the target is random. It was then propagated in the reverse direction back to the laser projection system's receiver. The propagation was through the same turbulent volume that the previous Gaussian beam had traversed. The aperture diameter of the laser projection system was 1.0 meter. The complex field captured by the system aperture was then passed through a centroid tracking tilt-removal system.

Finally, the tilt-removed complex field was propagated through an ideal lens which was used to form an image of the incoming wavefront. This far-field image was created by performing a FFT of the field just after the ideal lens. We used the image sharpness metric as the objective function and maximized it by finding the optimum set of α s. The optimization algorithm used in this case was the SPSA algorithm citation. We chose to use the SPSA algorithm because it converged much faster than the BFGS quasi-Newton algorithm. The simulation was done using a discrete form of the objective function in Eq.(7). The optimum α s are used to drive the deformable mirror and hence create to optimum phase correction. We used a trial and error method to determine the mask diameter, D_{mask} , that produce the best results in terms of encircled energy and radial energy. The values for θ_{mask} , ranged from $1.3479\mu\text{rad}$ to $74.136\mu\text{rad}$.

From Fourier optics,¹⁷ the spatial frequency, u , in the image plane is given by

$$u = \frac{x}{\lambda F}, \quad (11)$$

where x is the position scalar and F is the focal length. Therefore the sample spacing,

$$du = \frac{dx}{\lambda F}. \quad (12)$$

Also the frequency domain sample spacing in the fast Fourier transform (FFT) is given by

$$du = \frac{1}{Ndx}, \quad (13)$$

where N is the number of elements in the FFT. Therefore,

$$\frac{dx}{\lambda F} = \frac{1}{N dx} \quad (14)$$

and

$$d\theta_{mask} = \frac{dx}{F}, \quad (15)$$

where θ_{mask} is the angular extent of the mask aperture.

$$d\theta_{mask} = \frac{\lambda}{N dx} \quad (16)$$

$$\theta_{mask} = \frac{\lambda D_{mask}}{N dx}, \quad (17)$$

where D_{mask} is the diameter of the mask aperture. The angles were calculated using the following equation in discrete form,

$$\theta_{mask} = \frac{\lambda}{N \Delta x} D_{mask}. \quad (18)$$

Finally, the optimum corrected phase is added to the outgoing high power laser beam. This beam propagates through the same turbulent volume as the scattered light until it reaches the target plane. The intensity at the target plane is saved so that it can be used in the calculation of the percentage of encircled energy. We performed 20 independent realizations. Then we added the intensities in the target plane for each one of the realizations and calculated the ensemble average intensity. Next we performed a computation of the percentage of encircled energy from the ensemble average intensity. We used the percentage of encircled energy to measure the quality of the target image.

4. RESULTS

In this section, we present the results of the simulation described in Section 3. In each of the results presented below, $\theta_{mask} = 47.178 \mu\text{rad}$. For each of the figures below, the curve marked NLOPT refers to the results obtained using nonlinear optimization of the image sharpness metric and the curve marked HWFS refers to the results obtained using a Hartmann wavefront sensor and reconstructor and the curve marked NOCOMP refers to the results obtained without compensating for the atmospheric turbulence.

Fig. 3 shows a comparison of the percentage of encircled energy on the target using nonlinear optimization of the image sharpness metric, using HWFS processing and using no compensation are compared. The turbulence strength, $C_n^2 = 5.7354 \times 10^{-16} \text{ m}^{-2/3}$ and the Rytov number is 0.1262. The figure shows that for small angles, $\theta < 1 \mu\text{rad}$, the percentage of encircled energy is largest in the NLOPT case followed by the HWFS case and is smallest in the NOCOMP case. Therefore the NLOPT system concentrates more energy on a small area of the target than the HWFS and NOCOMP systems. The second performance metric, radial averaged target intensity, is shown in figure 4. Figures 3 and 4 show that at small angles, controlling the deformable mirror using nonlinear optimization-based techniques results in an improvement in percentage of encircled energy over controlling the deformable mirror using parameters obtained from a Hartmann wavefront sensor and reconstructor or not performing any compensation at all.

Figs. 5 and 6, show comparisons between the 3 systems, NLOPT, HWFS and NOCOMP when the turbulence strength, $C_n^2 = 9.5591 \times 10^{-16} \text{ m}^{-2/3}$ and the Rytov number is 0.2103. Fig. 5 shows that for small angles, $\theta < 1.5 \mu\text{rad}$, the percentage of encircled energy is largest in the NLOPT case followed by the HWFS case and is smallest in the NOCOMP case. Even with increased turbulence strength, the NLOPT system concentrates more energy on a small area of the target than the HWFS and NOCOMP systems. As in the previous figures above, Fig. 6 shows the radial averaged intensity at the target for the 3 systems. In each case the radial average energy drops as the we move away from the center of the target. The figure shows that the NLOPT system has the largest radial energy and most of it is concentrated in a small area close to the center of the target.

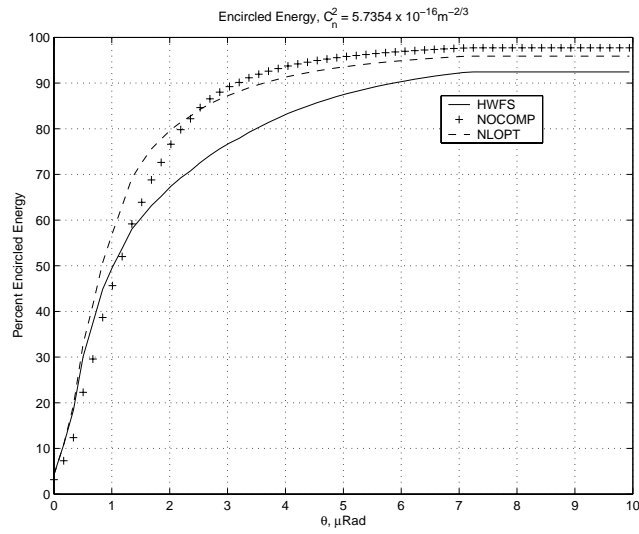


Figure 3. Percentage of ensemble average encircled energy in the target plane for $C_n^2 = 5.7354 \times 10^{-16} \text{ m}^{-2/3}$.

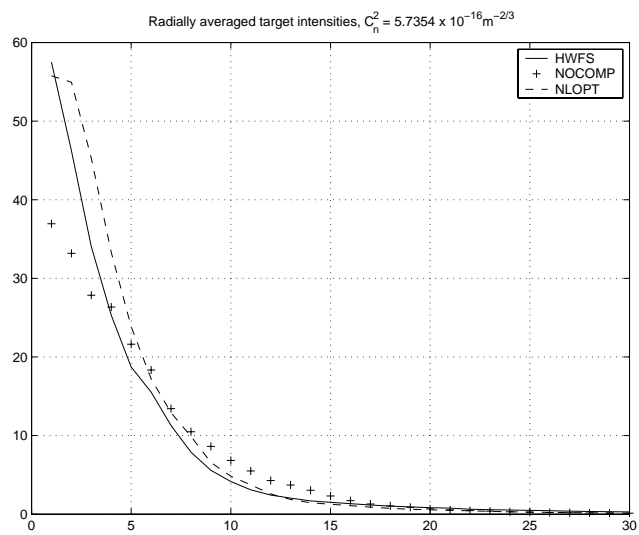


Figure 4. Average radial energy in the target plane for $C_n^2 = 5.7354 \times 10^{-16} \text{ m}^{-2/3}$.

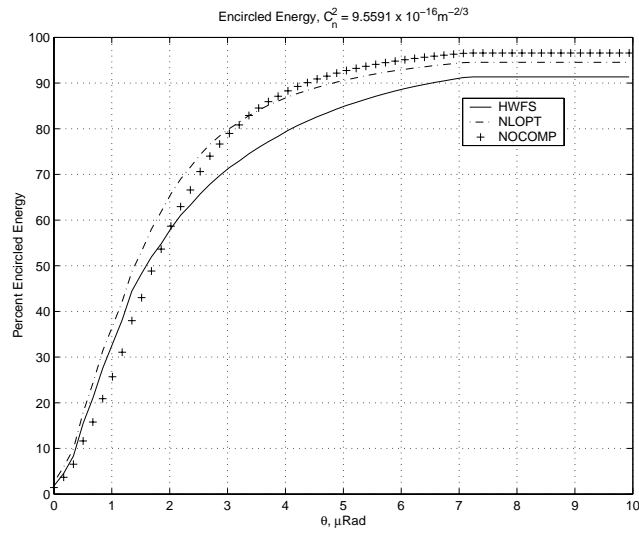


Figure 5. Percentage of ensemble average encircled energy in the target plane for $C_n^2 = 9.5591 \times 10^{-16} \text{ m}^{-2/3}$.

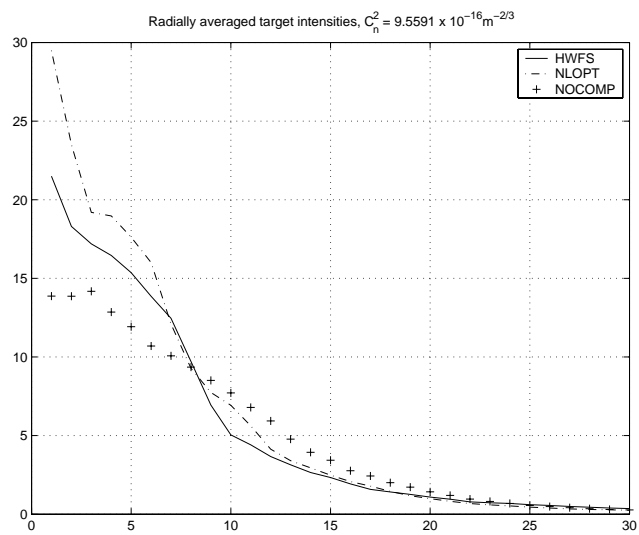


Figure 6. Average radial energy in the target plane for $C_n^2 = 9.5591 \times 10^{-16} \text{ m}^{-2/3}$.

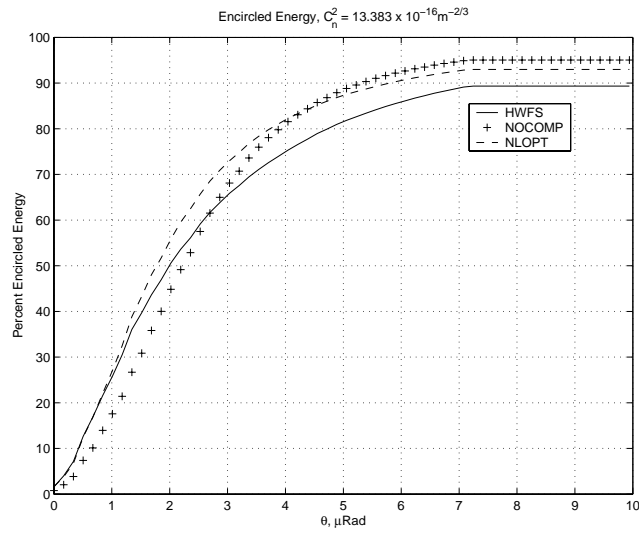


Figure 7. Percentage of ensemble average encircled energy in the target plane for $C_n^2 = 13.383 \times 10^{-16} \text{ m}^{-2/3}$.

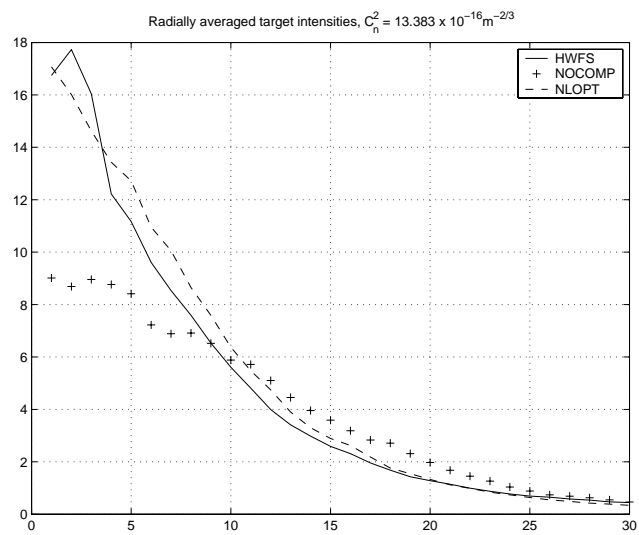


Figure 8. Average radial energy in the target plane for $C_n^2 = 13.383 \times 10^{-16} \text{ m}^{-2/3}$.

The comparisons between the NLOPT, HWFS and NOCOMP systems when the turbulence strength, $C_n^2 = 13.383 \times 10^{-16} \text{ m}^{-2/3}$ and the Rytov number is 0.2944 are shown in Figs. 7 and 8. Figure 7 shows that for small angles, $\theta < 2\mu\text{rad}$, the percentage of encircled energy is largest in the NLOPT case followed by the HWFS case and is smallest in the NOCOMP case. However at this level of turbulence, the performance of the NLOPT system is not significantly better than that of the HWFS system.

Table 1. Comparison of θ_{mask} with θ_0 for various Rytov numbers, σ_x^2

$C_n^2 (\times 10^{-16} \text{ m}^{-2/3})$	σ_x^2	$\theta_{mask} (\mu\text{rad})$	$\theta_0 (\mu\text{rad})$	θ_{mask}/θ_0
5.7354	0.1262	47.178	3.579	13.1818
9.5591	0.2103	47.178	2.6342	17.9032
13.383	0.2944	47.178	2.1527	21.916

Table 1 shows the ratio of θ_{mask} to the isoplanatic angle, θ_0 , for the 3 values of turbulence strength, C_n^2 , and Rytov numbers. The table shows that the angular subtense of the mask required to correct for turbulence can be many times larger than the isoplanatic angle. And as the turbulence strength increases and the isoplanatic angle decreases, the ratio θ_{mask}/θ_0 becomes larger.

5. CONCLUSION

A new approach to controlling a deformable mirror in beam projection systems operating in conditions of strong turbulence was introduced. It has been shown that the nonlinear optimization of an image sharpness metric can improve the performance of the beam projection system. However, in conditions of strong atmospheric turbulence, the radius of the mask's aperture was larger than expected and subtends an angle that could be 22 times larger than the isoplanatic angle.

REFERENCES

1. R. R. Parenti and R. J. Sasiella, "Laser-guide-star system for astronomical applications," *J. Opt. Soc. Am. A* **11**, pp. 288–309, 1994.
2. M. C. Roggemann and B. Welsh, *Imaging Through Turbulence*, CRC Press, Boca Raton, FL, 1996.
3. J. W. Hardy, "Active optics: A new technology for the control of light," *Proc. IEEE* **66**, pp. 651–697, 1978.
4. D. L. Fried, "Anisoplanatism in adaptive optics," *J. Opt. Soc. Am. A* **72**, pp. 52–61, 1982.
5. B. M. Welsh and C. S. Gardner, "Effects of turbulence induced anisoplanatism on the imaging performance of adaptive astronomical telescopes using laser guide stars," *J. Opt. Soc. Am. A* **8**, pp. 69–80, 1991.
6. M. A. Voronstov, G. W. Carhart, D. V. Pruidze, J. C. Ricklin, and D. G. Voelz, "Image quality criteria for an adaptive imaging system based on statistical analysis of the speckle field," *J. Opt. Soc. Am. A* **13**, pp. 1456–1466, 1996.
7. M. C. Roggemann and T. J. Schulz, "Algorithm to increase the largest aberration that can be reconstructed from hartmann sensor measurements," *Appl. Opt.* **37**, pp. 4321–4329, 1998.
8. M. C. Roggemann, T. J. Schulz, C. W. Ngai, and J. T. Kraft, "Joint processing of hartmann sensor and conventional image measurements to estimate large aberrations: theory and experimental results," *Appl. Opt.* **38**, pp. 2249–2255, 1999.
9. R. A. Muller and A. Buffington, "Real-time correction of atmospherically degraded telescope images through image sharpening," *J. Opt. Soc. Am.* **64**, pp. 1200–1210, 1974.
10. A. Buffington, F. S. Crawford, R. A. Muller, A. J. Schwemin, and R. G. Smits, "Correction of atmospheric distortion with an image sharpening telescope," *J. Opt. Soc. Am.* **67**, pp. 298–303, 1977.
11. D. A. Pierre, *Optimization Theory with Applications*, Dover Publications Inc., Mineola, NY, 1986.
12. M. A. Branch and A. Grace, *MATLAB Optimization Toolbox*, Math Works, Natick, MA, 1996.
13. J. C. Spall, "An overview of the simultaneous perturbation method for efficient optimization," *John Hopkins APL Technical Digest* **19**, pp. 482–492, 1998.

14. D. Fried, "Varieties of anisoplanatism," *Proc. Soc. Photo-Opt. Instrum. Eng.* **75**, pp. 20–29, 1976.
15. W. A. Coles, J. P. Filice, R. G. Frehlich, and M. Yadlowsky, "Simulation of wave propagation in three-dimensional random media," *Appl. Opt.* **34**, pp. 2089–2101, 1995.
16. J. M. Martin and S. M. Flatte, "Simulation of point-source scintillation through three-dimensional random media," *J. Opt. Soc. Am. A* **7**, pp. 838–847, 1990.
17. J. W. Goodman, *Introduction to Fourier Optics*, McGraw-Hill Book Co., New York, 1968.